Unstructured grid generation using LiDAR data for urban flood inundation modeling

Ryota Tsubaki†§ and Ichiro Fujita‡

Abstract. Inundation disasters, caused by sudden water level rises or rapid flow, occur frequently in various parts of the world. Such catastrophes strike not only in thinly populated flood plains or farmland but also in populated villages or urban areas. Inundation of the populated areas causes severe damage to the economy, injury, and loss of life; therefore, a proper management scheme for the disaster has to be developed. To predict and manage such adversity, an understanding of the dynamic processes of inundation flow is necessary because risk estimation is performed based on inundation flow information. In this study, we developed a comprehensive method to conduct detailed inundation flow simulations for a populated area with quite complex topographical features using LiDAR data. Detailed geospatial information including the location and shape of each building was extracted from the LiDAR data and used for the grid generation. The developed approach can distinguish buildings from vegetation and treat them differently in the flow model. With this method, a fine unstructured grid can be generated representing the complicated urban land features precisely without exhausting labor for data preparation. The accuracy of the generated grid with different grid spacing and grid type is discussed and the optimal range of grid spacing for direct representation of urban topography is investigated. The developed method is applied to the estimation of inundation flows, which occurred in the river basin of the Shin-minato River. A detailed inundation flow structure is represented by the flow model and the flow characteristics with respect to topographic features are discussed.

§ rtsubaki@hiroshima-u.ac.jp

1. Introduction

Inundation disasters, caused by sudden water level rises or rapid flow, occur frequently in various parts of the world. Such catastrophes strike not only thinly populated flood plains or farmland but also populated villages or urbanized areas. To predict and manage such adversity, understanding dynamical processes of inundation flow is necessary because risk estimation is carried out based on inundation flow information. Inundation disaster in populated areas causes damage to the economy, injury, and loss of life [Jonkman and Vrijling, 2008]; therefore, a proper management scheme for the disaster has to be developed.

The structures of the flow of the inundation of populated or urbanized areas are quite complex. In urban flooding, inundation water flows through street networks, and the anisotropy of the flow is quite strong. Consequently, the distributions of velocity and water depth show quite complex structures. To evaluate the inundation process properly in order to estimate the risk of house damage and human suffering, it is crucial to represent the local flow structure precisely. However, simplified models such as sub-grid modeling or reduced complexity modeling [Brasington and Richards, 2007] cannot represent flow structures in streets due to the limitation of the model resolution. Additionally, the sub-grid models need parameterization, but there is quite limited insight concerning the nature of the inundation flow in complex, actual urban topography because of the difficulty of the measurement and the complexity of the phenomena. An approach directly resolving the detailed flow structure by using a comparatively small scaled grid [Gallegos et al., 2009] is essential to predict the risk of structural damage and human suffering during flooding. To conduct the inundation simulation to resolve the detailed and complex flow structure, accurate and high-resolution topographical information is needed. The direct and detailed

inundation simulation approach demands more computational resources, compared with the adoption of the simplified approach. Furthermore, inundation risk assessment should be conducted in a stochastic framework, and a number of disaster scenarios should be investigated. The dimensions of the area under the risk of inundation is on the order of the size of a river basin. Additionally, the labor cost for data preparation is significant, so the automation of data processing and the optimization of data representation including the grid-size and the accuracy of land features (see Fig. 1) are needed.

In this study, we develop a comprehensive method to conduct detailed inundation flow simulations for populated areas using LiDAR (Light Detection And Ranging) data as the source of the land features information. Detailed geospatial information including the arrangement of each building is extracted from the LiDAR data; therefore, this method is applicable to rural or developing regions where GIS (geographic information system) land cover data are not available, but proper inundation disaster estimation is needed.

1.1. Geospatial data for flood inundation modeling

LiDAR has become an efficient alternative to traditional photogrammetric techniques because of its high potential for automation [Rottensteiner et al., 2002, 2003]. Raw LiDAR data itself is just a set of vast amounts of point location data (point-cloud), so some kind of data processing is needed to extract more useful, manageable and meaningful geospatial information. The LiDAR data processing can be categorized into three parts [Rottensteiner et al., 2002], namely

(i) Generation of a digital terrain model (DTM),

(ii) Surface cover (e.g. building, vegetation) extractions, and

(iii) Accuracy improvement methods for measured data.

Clode and Rottensteiner [2005] reported a classification method for trees and power lines by using first and last pulse information. For applications of 3-D city models, Vosselman [2003] presented methods for the reconstruction of a street network and locations of trees by using comparatively high resolution LiDAR data, here 0.1 m in resolution (distance between consecutive laser pulse) in the flight direction and 0.5 m in footprint size (diameter of a laser pulse at the ground surface) . Individual trees were detected by distinguishing their unique shape contained in the surface height distribution. Rottensteiner et al. [2003] presented an automated detection method for buildings, especially in residential areas using a combination of multi-spectral images and LiDAR data, whose resolution is comparatively low. Road extraction using remotely sensed data is also an important issue, especially for maintaining and revising GIS road information. Auclair-Fortier et al. [2000] reviewed the past research on road extraction for aerial and satellite monochromatic images. Sithole and Vosselman [2003] introduced a scan line segmentation method, to extract three-dimensionally connected road networks, which can be found around bridges and ramps.

To improve the quality of the geographical information for inundation simulation, LiDAR plays quite an important role because this measurement method improves not only the accuracy but also the spatial resolution of ground height information dramatically. The significant change in the measurement method led to a new research field for efficiently treating the huge amount of information obtained by LiDAR measurement [Bates, 2004]. Treatment of fine-resolution data obtained by LiDAR in inundation models is a state of the art technology involving not only hydrological insight but also remote sensing technology and efficient grid generation.

Priestnall et al. [2000] discussed how LiDAR devices can provide digital surface models for modeling flood inundation in urban and semi-urban environments. Cobby

et al. [2003] proposed a method for generating a grid for a finite-element discretization. In this method, to represent important land features such as hedges and trees accurately, an unstructured grid was used. First, river bathymetry was individually represented by a structured triangular grid. Then, the grid was connected smoothly to the floodplain by changing the grid size gradually using a distance matrix. Bates et al. [2003] explored the optimum assimilation of fine-resolution data into numerical models. To achieve this, significant length scales were estimated. Then, significant points were determined; subsequently, an unstructured grid was generated to represent land features to generate the topographically-optimum grid. Finally, sub-grid scale topographic information was incorporated into the model. They compared the results of topographically-independent (conventional and control), topographically-optimum and topographically-optimum with sub-grid correction. Rath and Bajat [2004] refer to expansion of use of LiDAR measurement, compare LiDAR and InSAR measurements, and represent an automated procedure to generate triangular unstructured grid for finite element flow simulation. The topographic feature they focused on was a break line, which represents a sequence of steep terrain slope patterns.

1.2. Vegetation modeling

The treatment of vegetation is also an important issue, especially when estimating dynamic processes of inundation flow precisely. Mason et al. [2003] modeled the flow resistance due to vegetation such as trees and crops. With this method, vegetation is classified into three categories; short vegetation (height less than 1.2 m), tall vegetation (height greater than 5.0 m) and intermediate vegetation (from 1.2 m to 5.0 m). They concluded that little difference could be detected between the constant friction model and the variable friction model; however, the impact due to the difference of the models on the dynamical process of inundation (e.g., time-series of local velocity) is

not understood well.

Mason et al. [2003] adopted spatial filtering to classify surface properties such as height of vegetation. The DTM was estimated using a statistical (empirical) relationship between height and surface roughness in the short vegetation regions and interpolated from surrounding height in tall and intermediate vegetation regions. However, the floodplain, which they studied, was rural, so no attempt was made to distinguish buildings from trees, as there are generally few buildings in a rural floodplain.

1.3. Urban flood inundation modeling

Detailed urban flood modeling is a rapidly developing research field. Yu and Lane [2006a,b] modeled flood flow around an urbanized area with high-resolution land feature information employing an efficient and rational modeling procedure. They used a 2D diffusion-wave model based on a raster (Cartesian) grid and discussed grid resolution effects [Yu and Lane, 2006a] and the validity of introducing a sub-grid topographical model [Yu and Lane, 2006b]. McMillan and Brasington [2007] also estimated the accuracy and calculation efficiency of the sub-grid modeling using a 10-m Cartesian grid. They reported that their approach offered a reasonable result with little computational cost compared with a fine grid model without sub-grid modeling. Schubert et al. [2008] reported an unstructured grid model for urban flooding. They used a comparatively fine grid in the range of 0.8 m to 10 m to represent building shapes and vegetation cover explicitly. They estimated the sensitivity to flood propagation due to changes of building treatment and surface friction modeling. Sanders et al. [2008] developed an urban flood model by considering anisotropic porosity to model sub-grid effect. They used an unstructured grid for spatial discretization and compared results calculated using their porosity model with different drag coefficient modeling effects of sub-grid topographical features, direct building representation models with a finer grid, and experimental results

[Testa et al., 2007] with different building modeling. Hunter et al. [2008] conducted benchmark testing of six two-dimensional hydraulic models with the Cartesian grid system. They also estimated the sensitivity of topographical representation and friction parameters and concluded that uncertainty in friction parameters becomes a more dominant factor than topographical error for fine grid inundation simulation.

As described above, the methodology for detailed and precise urban flood modeling has been discussed in several approaches; however, each method seems to have both advantages and disadvantages, and it is therefore difficult to determine the best method, which may depend on the objective of the simulation (e.g., Schubert et al. [2008]). Fine grid modeling with direct building representation seems to yield a certain benchmark value (e.g., Mason et al. [2007], Schubert et al. [2008]). Sub-grid parameterization approaches may be also capable of obtaining the flow information as accurate as fine and detailed modeling approaches; however, to achieve this, sub-grid approaches need quite sophisticated and complex parameterization including a number of fitting parameters. Due to the limitation of the understanding of inundation flow nature, the sub-grid approaches may have larger uncertainty for the dynamic process of inundation in urban area.

The inundation extent is comparatively easy to observe and to record, and of course, quite important information to estimate damages due to inundation. The mass conservation is the most important aspect to predict the maximum inundation extent, and sub-grid (e.g., Yu and Lane [2006b], Sanders et al. [2008]) or reduced-complexity (e.g., McMillan and Brasington [2007]) approaches mainly depict the mass continuity in detail using comparatively large-scale grids. However, up-scaling or integration of the momentum conservation is remarkably difficult and complicated and not yet understood well. The momentum source and sink depend on local flow structures, but the sub-grid

approaches can not resolve local flow structure directly.

1.4. Study objectives

In this study, a topographical model for numerical simulation is generated using land features obtained by LiDAR survey and aerial photographs. The ground height distribution as well as the arrangement of buildings and vegetation cover is obtained by a single surveying flight.

There is dataset of a city map, containing individual building shapes, generated and updated using the aerial photographic survey and the field survey. This conventional building dataset provides reliable building arrangement information, and thus the combination of LiDAR measurement and GIS map data may be reasonable for practical use (e.g., Hunter et al. [2008]); however, consistency of information between LiDAR data and GIS maps cannot always be achieved due to the differences in the survey or update dates. Detailed and most recent building arrangement information can be obtained within a limited region, and even if available, this can be expensive in some cases due to the high cost of surveying and revising. Additionally, details on the vegetation, e.g., dimensions and growth status, are not recorded in prevalent GIS (Schubert et al. [2008]); however, this information is quite important to estimate the flow resistance.

In this study, we report a number of data processing schemes designed to support urban flood inundation modeling with unstructured grids. Unstructured grids allow for a precise depiction of building walls, over a wide range of grid resolutions, in comparison to Cartesian grids (e.g., Schubert et al. [2008]). However, the generation of constrained unstructured grids can be time consuming, which limits the appeal of such methods for hydraulic engineering practice. To address this problem, we describe semi-automated methods of generating unstructured grids from high resolution LiDAR data.

To represent rapid inundation flow on a populated area, it is important to specify

ground height distribution, building configuration, and vegetation cover accurately [Schubert et al., 2008]. A height distribution can be obtained directly from LiDAR. Building configuration and vegetation cover are also obtained from data processing from LiDAR and the orthophoto. Then, an unstructured grid containing representative land features was generated using the advancing front method [Lo, 1984]. By using this method, actual inundation disasters that occurred in an urbanized area are simulated, and the calculated result is compared with the disaster record.

2. Methods

To estimate the inundation flow in a populated area, the effect of detailed land features (Fig. 1) on the inundation flow must be modeled properly, especially to resolve the dynamic processes of inundation. Not only precise but also rational and efficient treatment of geospatial information is essential for practical use. In this section, a set of procedures to obtain a detailed topographical model for inundation simulation is presented. The quality of the generated grids, with different grid sizes and grid systems, are evaluated. Finally, the flow model used in this study is described.

2.1. Geospatial data treatment

A flowchart of the procedure we developed to obtain an unstructured grid for flow calculation is shown in Fig. 2. Table 1 summarizes the conditions of the LiDAR data used in this study. The process of each step in a sample area is depicted in Fig. 3. The first step is to prepare the ground area from a directly observed digital surface model (DSM; Fig. 3b). The separation of ground point elevation from overall observation data is called filtering (Weng and Quattrochi [2006]). From the extracted ground point data, the digital terrain model (DTM) is interpolated. In this study, the line segmentation

approach, proposed by Sithole and Vosselman [2003], is used to obtain DTM. This method involves the segmentation of a point-cloud (a large number of raw data points obtained by LiDAR measurement) followed by a classification. Based on local slope between neighboring points, the domain is segmented by elevation discontinuity. Then, based on the elevation connectivity of the neighboring segments, the domain is classified as

(i) terrain (bare earth and attached objects such as bridges and overpasses, which connect to bare earth on one side),

(ii) detached objects (buildings and vegetations), and

(iii) unclassified area,

so this method is better adapted to the unique land features of urbanized areas. In this study, to treat the river channel and the entrance of the underpass, a concave area is introduced. In Fig. 3c, the results of the scan line segmentation are shown. The DTM (Fig. 3d) is obtained by the interpolation of the height of the surrounding ground surface. A convex region is extracted, as shown in Fig. 3e. This region contains both a building area and vegetation region; however, the hydraulic properties of building and vegetation cover are not identical, so we should treat them separately. Vegetation cover makes it difficult to identify buildings wall when buildings and vegetation are located adjacently to one another.

In order to distinguish between vegetation and building areas, we first tried to use height information such as the shape detection technique [Vosselman, 2003] and the difference between the first and last pulse heights [Clode and Rottensteiner, 2005], but it was found that those approaches do not work well for our site because the point density in our case is about 1 point/m^2. It is not sufficient to distinguish vegetation and buildings using LiDAR data only because of

- the shape of a small house is difficult to distinguish from that of a tree,
- trimmed shrubberies are designed with varied shapes or have no specific shape, and
- trimmed shrubberies show a small difference between the first and last pulse height because of the outer leaves pruning.

To overcome the difficulty in distinguishing buildings from vegetation using only height information, we utilize the combined information of height and color to detect buildings and vegetation as in the multi-spectral approach [Rottensteiner et al., 2003]. The normalized difference vegetation index (NDVI) is widely used to extract the area and status of vegetation. In this study, unfortunately, the near infrared spectral image was not obtained in the measurement. Thus, we use true color orthophoto recorded by a high-resolution digital camera during the LiDAR measurement. Threshold of color range of vegetation area is determined using the Adobe Photoshop CS3 software, and whole area is divided into vegetation or non-vegetation areas. A spatial filter is then applied to smooth the spatial scattering of the vegetation mask boundary (see Fig. 3f). The logical product of the vegetation mask and the convex region mask is treated as a vegetation area, and the logical product of negative the vegetation mask and the convex region mask is treated as a building area.

2.2. Extraction of building outline

The commonly used resolution of LiDAR measurement for large extent is one to two meters [McMillan and Brasington, 2007]. By using an unstructured grid, it is possible to represent the major land features in the grid system in which the grid size is larger than one to two meters. Now, we should extract the essential properties of geospatial information obtained by LiDAR and express these features using an unstructured grid.

The unstructured grid generation technique was developed mainly in the field

of structural evaluation, aerospace research and computer graphics to treat complex geometry [Owen, 1998, Teng and Wong, 2000, Lo, 2002]. There are two fundamental, major approaches to generate an unstructured grid, namely Delaunay triangulation and the advancing front method (AFM) [Hoffmann and Chiang, 1993, Kaneko et al., 2000]. In the former approach, grid nodes are distributed in the domain, and therefore the points are connected to form each grid cell by using Delaunay triangulation. This method is designed to provide an efficient procedure for connecting a given set of points into an optimum unstructured triangular mesh. This method is efficient and generates a comparatively good quality triangular mesh. This method essentially cannot treat domains contains concavities (see Fig. 4a, b), so that extra and symptomatic treatments are required to treat complex domain shapes including multiply-connected boundaries (see Fig. 4c). In the latter approach, namely AFM, the boundary of the domain is formed by using connected grid nodes; thus, the grid cells are put beside boundary interfaces into the inner region, just like tiling a floor. This method is comparatively simple and easy to implement. Additionally, this method can treat concave domains without any difficulty or additional effort, and it is easy to treat multiply-connected domains [Hoffmann and Chiang, 1993].

This study focuses on inundation flow in an urbanized area, where the arrangement of the buildings and road network is one of the dominant factors for the inundation flow [Gallegos et al., 2009]. We need to treat domains containing concave and multiply-connected boundaries, and so we select AFM for the grid generation scheme.

To represent a road network accurately with a smaller number of grids, it is important to generate a grid system that represents the building boundary shapes precisely. To achieve this, the building extraction from LiDAR data should be implemented. A building extraction technique, used for mapping and city modeling

purposes, usually consists of three sequential steps, namely

(i) segmentation of the domains that belong to the same building,

(ii) tracing building boundary shape, and

(iii) regularization of the boundary [Weng and Quattrochi, 2006, Sampath and Shan, 2007].

As a result, shape of each building is represented as a horizontal polygon (or three-dimensional object in the case of city modeling). Both the accuracy of the boundary shape and the conciseness of the polygon representation are the focus of developing the building extraction method for mapping and city modeling purposes. In this context, the lengths of line segments constituting the building boundary polygons are not restricted.

In this study, the building boundary polygon is used for the flow boundary condition. To conserve the void ratio (occupation ratio of the building area in a specific area) of the inundation extent and to represent the inundation water flowing through the street network, precise representation of the building boundaries is needed. The calculation grid is generated using the building boundary polygon shape. Inhomogeneity of size and shape of triangles composing the grid reduced stability and efficiency of the flow calculation. To obtain the calculating grid with small inhomogeneity of grid, conciseness of building boundary polygon is important. This is because, for example, to represents 0.5 m line segment in the building boundary precisely, triangle, 0.5 m on a side, should be generated. However, lengths of line segments composing the building boundary are not constant and cannot be represented by multiple number of the specific value. To generate the grid with small inhomogeneity, lengths of the building boundary line segment should be larger than the grid size. In this study, the highly developed residential and commercial area, consisting of a number of commercial buildings (having dimensions of several dozen meters), a large number of small houses

(on the order of one or a dozen meters), and vegetation besides buildings, is treated. The complexity of the land features of the area treated in this study is high compared with the topography treated in the conventional building modeling studies, e.g., in Brenner [2005], H. Kaartinen et al. (twelve authers) [2005], Sampath and Shan [2007]. To achieve these demands, a simple, robust and reasonably accurate building extraction method should be implemented.

The building extraction technique can be separated into three steps as described previously. In the first step, building segmentation can be easily implemented using the building mask obtained by a Boolean operation of the convex region mask and the vegetation mask (Fig. 3e and f). In the second step, the building boundary tracing is implemented as follows. Here, the outline of each building is extracted from the building raster mask $M(x, y)$ =0 or 1 (shown in Fig. 3e). Each edge of the building outline is extracted using the following procedure. First, the outline of each independent building in the mask is obtained by clockwise (or anti clockwise) tracing of the outline (boundary between $M = 0$ and $M = 1$). The outline is treated as a series of location point vectors ($\boldsymbol{P}_i = (x, y) : i$=0.. i_{max}). Second, the local curvature θ_i is calculated by using vector $\boldsymbol{P}_i - \boldsymbol{P}_{i-3}$ and $\boldsymbol{P}_{i+3} - \boldsymbol{P}_i$ as shown in Fig. 5a for $i = 4$ and Fig. 5b for $i = 7$. Then, the location of the edge is assumed to be the intersecting point of line $\boldsymbol{P}_{i-4}\boldsymbol{P}_{i-1}$ and line $\boldsymbol{P}_{i+1}\boldsymbol{P}_{i+4}$ as shown in Fig. 5c for the sample for $i = 7$. Using the same process explained above, we can obtain a series of edge points as shown in Fig. 6b from building mask (Fig. 6a). An offset value of 3 for i achieves both accuracy and stability of shape detection by trial and error in this study.

To represents a rounded shape, which contains no edge points, the intermediate points are added on the condition that the distance between the original outline and polygon boundary becomes larger than some specific value. In this study, a value of 2 m

is used as the criterion to add the intermediate points. Thus, the boundary shape error between building mask and building polygon is smaller than 2 m in horizontal distance.

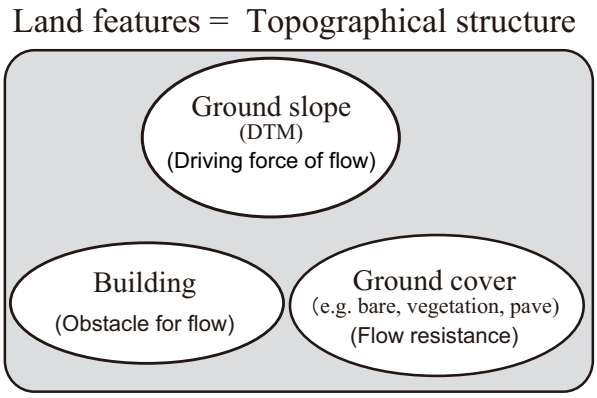

Figure 1. Definition of land features and these roles on inundation flow.

Table 1. Summary of used LiDAR data

Date	9. Sept. 2004
Platform	Cessna C207
Laser scanner	ALTM3100-C (Optec)
Laser pulse frequency	50 000 Hz
Altitude	2000 m
Scanning angles	$\pm 12^{\circ}$
Scanning frequency	30 Hz
Flight velocity	60 m/s
Over lap	20% (average)
Point density	$1/m^2$
Flight course	8

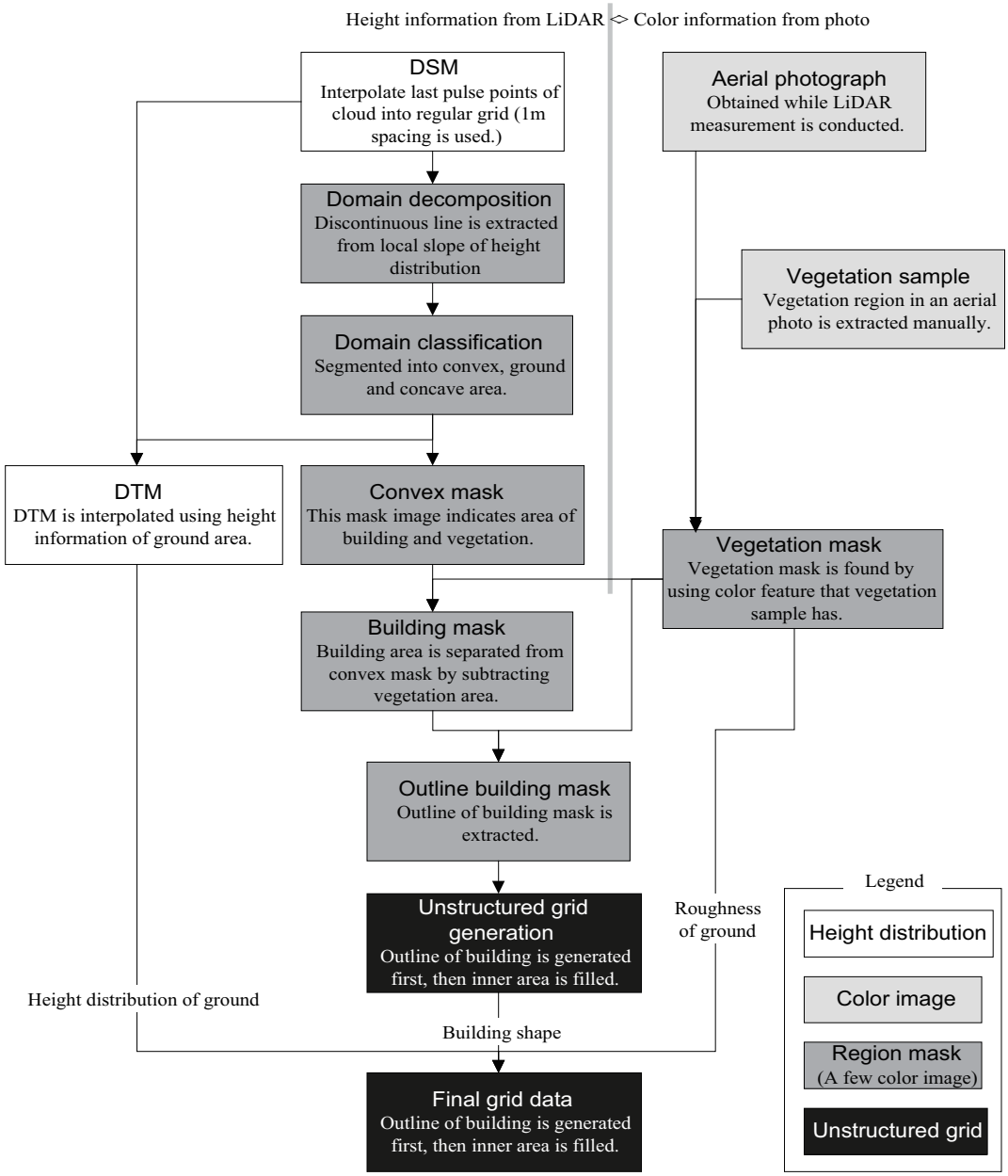

Figure 2. Flow chart showing main stages of data processing.

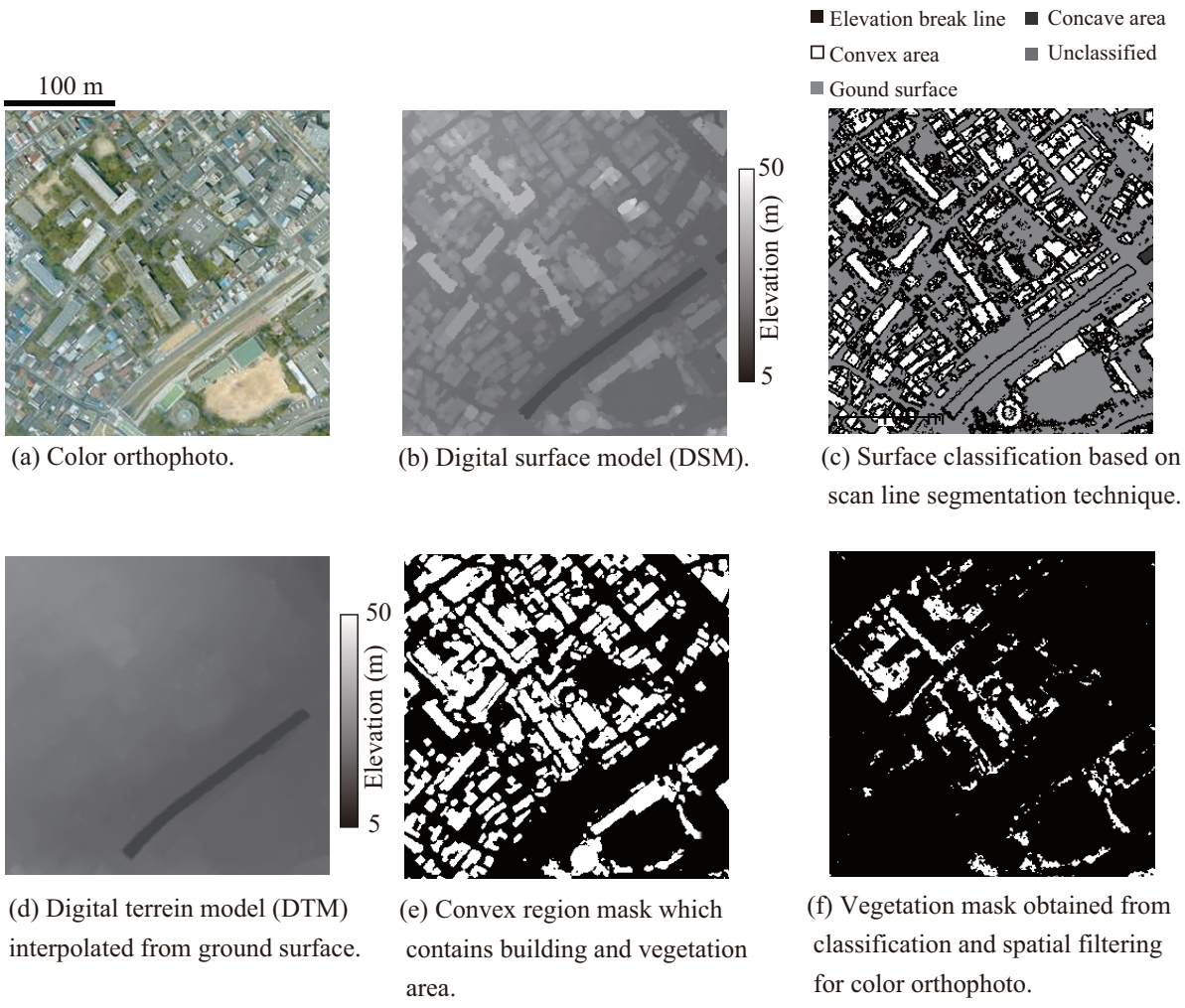

(a) Color orthophoto.

(b) Digital surface model (DSM).

(c) Surface classification based on scan line segmentation technique.

(d) Digital terrein model (DTM) interpolated from ground surface.

(e) Convex region mask which contains building and vegetation area.

(f) Vegetation mask obtained from classification and spatial filtering for color orthophoto.

Figure 3. Steps of LiDAR and color data processing.

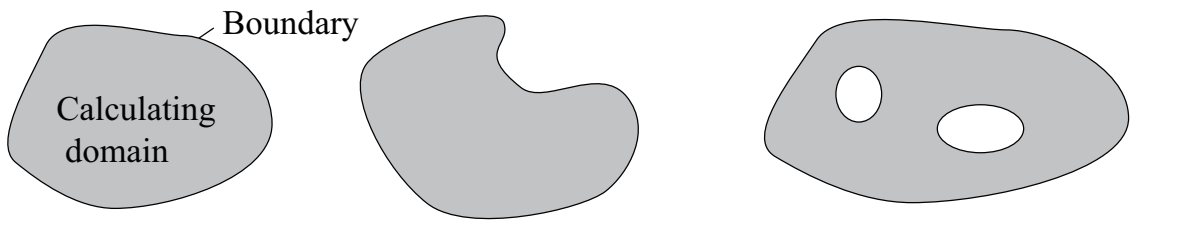

(a) Convex domain (b) Domain contains concave (c) Muilitply-connected domain

Figure 4. Domain types.

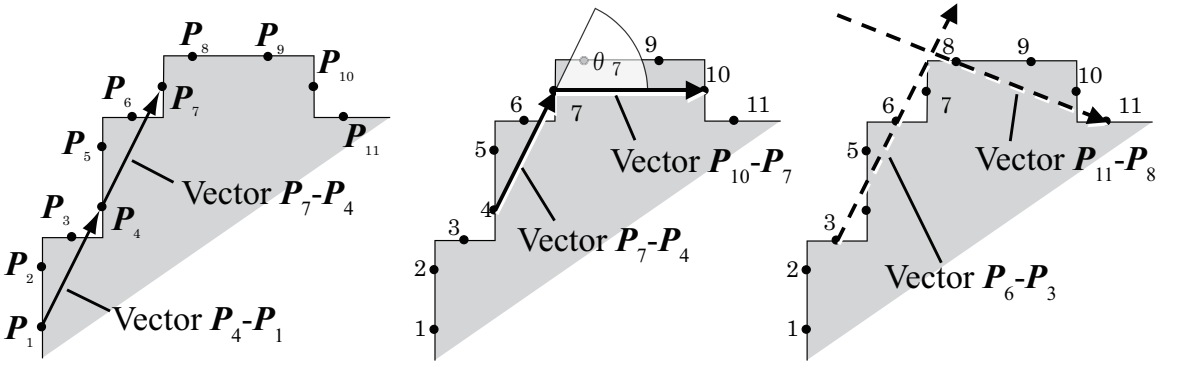

(a) Searching for edge. (b) Nominated point of edge. (c) Estimation of location of edge.

Figure 5. Edge detection from a series of points.

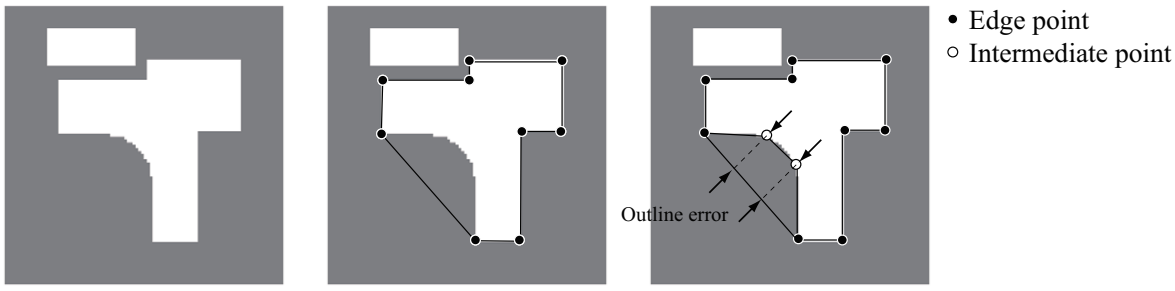

(a) Original building shape. (b) Edge points are detected by local maximum of local curvature. (c) Intermediate points are added to the location where outine error is larger than threshold (2 m in this study).

Figure 6. Extraction of outline.

2.3. Unstructured grid generation

Fig. 7a and Fig. 7b show the orthophoto and GIS map of the sample area. In this area, small residential houses, school buildings and commercial facilities are densely packed with roadside trees and shrubberies present between buildings. In the aerial photograph, vegetation can be seen in some places, and this information is not recorded in the GIS map. Fig. 7c shows the extracted outline of buildings. Based on this building outline, the inner grid is generated using AFM [Kaneko et al., 2000]. In the AFM, boundary cells (or sides) are arranged first. Inner cells are then generated as follows: Along the boundary (initial front; Fig. 8a), a new triangle (new front) is generated by adding a new grid node as shown in Fig. 8b. The triangles are formed one after another (Fig. 8c). In some cases the grid nodes, which are already set, are used to form other triangles (Fig. 8d). Triangles are formed with and without adding a new point (front advancing to inner area), and finally the entire domain is filled up with triangles.

It is rare that any mesh generation algorithm will be able to define a mesh that is optimal without applying some kind of post-processing to improve the overall quality of the generated grid [Owen, 1998]. The generated grid contains some amount of long thin triangles as shown in Fig. 8. The thin triangle cells cause a reduction of the accuracy and stability of the numerical flow simulation. Therefore, Laplacian smoothing [Field, 1988, Canann et al., 1998] is applied as post-processing to improve the overall quality of the grid. The Laplacian smoothing is an averaging method, and the simplest and most straight forward mesh smoothing algorithm. With this method, an internal grid point is placed at the average location of any grid points connected to it [Owen, 1998]. Fig. 8g shows a sample of the result of the smoothing applied to the original grid (as shown in Fig. 8f).

After the whole domain is filled with cells, the local ground roughness and elevation

is attributed to each cell. The friction for flow is estimated using Manning's friction parameter n. $n_g = 0.01$ is used for ground surface area, and $n_v = 0.1$ is used for the vegetation region [Woolhiser et al., 1990, Schubert et al., 2008]. If the ground surface and vegetation area exist in the same cell, parameter n is calculated considering a fraction of ground area A_g and vegetation area A_v as follows:

$$n = \left(\frac{A_g n_g^{3/2} + A_v n_v^{3/2}}{A_g + A_v} \right)^{2/3} . \tag{1}$$

This is derived from $u = \frac{1}{n} R^{\frac{2}{3}} I^{\frac{1}{2}} = \frac{1}{n_v} R_v^{\frac{2}{3}} I^{\frac{1}{2}} = \frac{1}{n_g} R_g^{\frac{2}{3}} I^{\frac{1}{2}}$, $R = A/S, R_g = A_g/S_g, R_v = A_v/S_v, A = A_g + A_v$, and $S = S_g + S_v$ [on Hydroscience and Hydraulic Engineering, 2000]. The generated unstructured grid with roughness information is depicted in Fig. 7d. The elevation of each cell is calculated by averaging the heights of the DTM elevation within the cell domains.

2.4. Grid evaluation

In this section, the spatial representation errors of the generated grids are evaluated to understand the effect of the grid types and sizes on the geometric error of the generated grids. Fig. 9 shows sample of the actual building raster, generated grid sample, and the error of two different sample grids. A one-meter building mask raster, obtained in section 2.1, is assumed as correct data herein. The property of each pixel in the correct raster is compared with the property of the grid cell that includes this raster point within the cell domain. By comparing the correct building raster and the generated grid, the area can be categorized into four parts, namely;

(i) True building, actual building area represented as building area in the grid.

(ii) False building, ground area but represented as building. This error induces a blockage effect on the flow due to the reduction of flow capacity.

(iii) True ground, actual ground area represented as ground in the grid.

(iv) False ground, building area but represented as ground. This error yields an underestimation of the obstruction of flow by the building because the shape of the building represented in the grid is smaller.

Fig. 9b is a sample of a grid, generated without considering the location of edge points, but the boundary cells have an approximately constant grid size. In a sense, this constant grid size approach is superior from the view point of numerical discretization for accuracy and stability; however the accuracy of topographical representation, in particular building boundaries, is significantly low. Fig. 9d is a grid generated with grid nodes distributed on each edge point of a building. As compared with Fig. 9c, false ground and false building errors are drastically reduced by arranging grid nodes at edge points. As described in section 2.2, the edge points and the intermediate point are independently treated in this study to represent the building outline in the grid with a small horizontal error. To evaluate the dependency of grid sizes and types on the spatial representation error, grids with eight different grid sizes, from 3 m to 25 m, are generated. Cartesian grids with the same grid size range are also generated in order compare grid representation characteristics of a structured grid, as this type of the grid is widely used in inundation simulation (e.g., Hunter et al. [2008].) In the Cartesian grid used herein, over 50 % of the domain is occupied by the ground surface, and defined as a ground cell. The building cell is the cell whose area is occupied over 50 % by the building area.

Fig. 10 shows a domain used to evaluate grid accuracy of different grids. As shown in this figure, small residential and commercial structures are densely distributed, and complex topography is observed in this area. The details of the generated grids are compared in Fig. 11. In the case of a coarse Cartesian grid (Fig. 11a), both false ground and false building errors are observed all over the domain. Detailed

topographical features as well as general structural aspects are not reproduced with the coarse grid system. The medium sized Cartesian grid (Fig. 11b) shows a better representation of the topography compared with the coarse Cartesian results; however, the blockage of small passages between buildings is observed at several points. This means that, without considering sub-grid topography modeling, the inundation flow network is not represented by the Cartesian grid with a grid size of roughly 10 m. In the fine Cartesian grid (Fig. 11c), detailed topographic features are generally represented well; however, step-like boundary shape error is observed around the boundaries of buildings. Unstructured grid results also reduce two kinds of errors in proportion to the reduction of grid size. A coarse unstructured grid (Fig. 11d) contains significant errors, and topography is not represented in detail. However, the blockage of small passages (false building error) is much less than that of the coarse Cartesian grid with the same grid size. In the medium sized unstructured grid (Fig. 11e), the general structure of the buildings and the road network are properly reproduced, so by using this range of the grid size, a general structure of the inundation flow network can be represented. Finally, in the fine unstructured grid (Fig. 11f), both building arrangements and road network are represented fairly well. In the fine unstructured grid, unsurprisingly, boundaries of buildings are represented most precisely.

It is possible to improve the building boundary representation using the coarse grid by using local refinements around buildings. However, in urban inundation prediction, not only building shape but also representations of roughness and local ground slope are essential, and the representation of the latter factors is also related to grid resolution. Additionally, the inhomogeneity of grid size and shape reduces the computational efficiency [Schubert et al., 2008]. Thus, in this study, to consistently maintain the resolution of building boundaries, roughness distribution and ground slope resolution,

the homogeneous grid size is used, and consequently, the representation of buildings is coarse because the grid resolution is decreased.

Fig. 12 compares the errors for each grid system. In general, grid error decreases almost proportionally to the reduction of the grid size. The false building error of the structured grid seems to approach some constant value in the larger grid size range (over 10 m). This may be because the horizontal topographical features, namely the configuration of the road network and buildings, have a spatial scale of about 10 meters in this area. In the range of under 10 m grid size, the representation of topography is improved by using a smaller grid size in the Cartesian grid; however, for grid sizes of more than 10 m, fundamental topographic features are not represented at all, and the accuracy is not influenced by changes of grid size in the Cartesian grid. In the range of less than 10 m for Cartesian grids, the magnitudes of false ground areas and false buildings are of the same order and decrease proportionally to the grid size. This is because the step-like error of the boundary becomes a dominant source of error. For the same grid size, errors in the unstructured grids are smaller than those of Cartesian grids. In general, both the false ground area and the false building area in unstructured grids are reduced proportionally to the grid size. The order of the false building error is about one third that of the false ground area. The false building area becomes a cause of blockage effects in the flow on the streets. In order to represent the flow network shape, a representation of the passage between buildings is important. With this in mind, an unstructured grid with a 13-meter grid size can resolve flow structure, which is comparable to a 3-meter Cartesian grid without subgrid model because the magnitude of false buildings of the former is of the same order. In other words, to represent both intricate building arrangements and road networks, an unstructured grid is reasonable from the view point of grid efficiency. It is difficult to determine the optimal unstructured

grid size only from Fig. 12 because the result does not show a clear inflection point in the plot of grid error with different grid sizes. However, a range of 1 to 5 meters appears to be the order of spatial resolution in Cartesian grids necessary to accurately represent urban topography [Djokic and Maidment, 1991, Mark et al., 2004, Hunter et al., 2008]. With this estimation, and considering the low blockage error (false building error) for topographical representation using an unstructured grid, 3 to 8 meters is a reasonable range for urban inundation flow estimation using an unstructured grid.

2.5. Flow model

Many researchers have developed numerical inundation propagation models. Owing to these developments, modern numerical methods achieve accuracy, stability and efficiency (e.g., Alcrude and Garcia-Navarro [1993], Tamamidis and Assanis [1993], Anastasiou and Chan [1997], Wang and Liu [2001], Shigeda et al. [2002], Bates et al. [2003]). In addition, the model physics and numerical methods (e.g., shock capturing and free surface treatment) have become sophisticated. In this study, two-dimensional shallow-water equations are solved using a shock-capturing finite-volume scheme using the unstructured triangulate grid system.

2.5.1. Basic equations and discretization In this study, the following basic equations are used.

$$\frac{\partial h}{\partial t} + \frac{\partial hu}{\partial x} + \frac{\partial hv}{\partial y} = 0, \tag{2}$$

$$\frac{\partial uh}{\partial t} + \frac{\partial u^2 h}{\partial x} + \frac{\partial uvh}{\partial y} + \frac{g}{2}\frac{\partial h^2}{\partial x} - gh\frac{\tau_{sx} - \tau_{bx}}{\rho} = 0, \tag{3}$$

$$\frac{\partial vh}{\partial t} + \frac{\partial uvh}{\partial x} + \frac{\partial v^2 h}{\partial y} + \frac{g}{2}\frac{\partial h^2}{\partial y} - gh\frac{\tau_{sy} - \tau_{by}}{\rho} = 0 \tag{4}$$

where h is depth of flow, u and v are depth-averaged velocity components in the x and y directions, t is time and g is gravitational acceleration. τ_{bx} and τ_{by} are related to the

bed slopes in the x and y directions and τ_{sx} and τ_{sy} are bed shear stresses. They are defined as

$$\frac{\tau_{bx}}{\rho} = -\frac{\partial z_b}{\partial x},\ \frac{\tau_{by}}{\rho} = -\frac{\partial z_b}{\partial y},\ \frac{\tau_{sx}}{\rho} = \frac{n^2 u\sqrt{u^2+v^2}}{h^{4/3}},\ \frac{\tau_{sy}}{\rho} = \frac{n^2 v\sqrt{u^2+v^2}}{h^{4/3}} \tag{5}$$

where n is Manning's roughness coefficient, and z_b is the local bed elevation.

The finite volume method is used to discretize the basic equations in the same manner used by Shigeda et al. [2002], Shige-eda and Akiyama [2003]. The flux difference scheme is adopted to discretize the advection and the source terms of the basic equations. The flow parameter is defined at the center of each cell, and a flux difference scheme is introduced to achieve numerical stability. The boundary of buildings is treated as a slip wall condition.

3. Shin-minato River inundation disaster

In this section, actual inundation disasters that occurred in an urbanized area of the Shin-minato River basin in Kobe City, Hyogo, Japan are simulated using the method developed in the present study. In section 3.1, a summary of the river and the situation of flood sufferings are described. In section 3.2, the inundation simulation considering complex topography using 5-m grid spacing is conducted to represent inundations that occurred in 1998 and in 1999. Calculated results are compared with the actual inundation situation and the structure of inundation flow is discussed.

3.1. Outline of the site

The Shin-minato River system retains a river basin of 35 km^2 in area, rising at Mt. Futatabi and converging with several tributary streams, and flows through Kobe city then pours into the Osaka bay [Hyogo prefecture, Japan, 2000, 2001]. The length of the main river system is 12 km. The downstream area of the Shin-minato River is

almost urbanized and has residential, commercial and industrial uses. Due to high production rate of sediment in this river system, in the downstream area, the river bed and surrounding ground have been aggradated gradually due to the periodical flooding. The severe flood in 1896, caused a 100-m dike breach, and 117 houses destroyed with 38 deaths. After this disaster, the river path in the downstream area was changed to enlarge the width of the cross-section and the capacity of flood discharge. The topography of the area and location of the Shin-minato River and its former path are shown in Fig. 13. Despite this change of the river path in 1967, the river basin suffered severe inundation with 84 deaths, and since then the flood control policy and design of the river have been revised. In 1995, the South Hyogo Prefecture Earthquake struck Kobe city, and the river bank and structure of the Shin-minato River were severely damaged. To recover this damage and to increase flow capacity, a recovery project was conducted. During this project, in 1998 and 1999, the Shin-minato River suffered huge floods with overflows occurring almost at the same location, and the surrounding areas were inundated (see the inundated area and the overflow point shown in Fig. 13.)

The disaster in 1998 was trigged by a typhoon passing through the area. The maximum flow discharge was estimated to be from 130 m^3/s to 140 m^3/s. At this time the flow capacity of the Shin-minato River was designed to be only 100 m^3/s. In addition, temporary constructing structures for earthquake damage recovery were installed in the river bed thus reducing the actual flow capacity, and this led to overflow starting from a discharge of 80 m^3/s. Debris and driftwood became lodged around the temporary structures in the river during the flood and reduced the capacity of the river to as little as 50 m^3/s to 65 m^3/s after passing the flood [Kobe Shimbun (news paper), 1999c].

In the following year, in 1999, the local heavy rainfall caused by a strong rain front

triggered a flood and overflow at the same location. At that time, restoration work had been completed and there were no temporary structures in the river, so the capacity of the river was about 130 m^3/s [Kobe Shimbun (news paper), 1999a]; however, overflow occurred again because of the large peak flow rate of the flood, estimated as 160 m^3/s to 170 m^3/s [Kobe Shimbun (news paper), 1999c].

3.2. Estimation of inundation disasters

3.2.1. Calculation conditions The calculation domain used in this study has an area measuring 1600 m by 1600 m, around the overflowing point. In Fig. 14, the DSM and the DTM are shown. In this figure, we can confirm that the elevation of the ground around the river and the former river path (locations are shown in Fig. 13) are locally high. This is due to high sediment deposition supplied from the river in the past.

LiDAR data used in this study were measured in 2004. Comparing the 2004 topography with that of the topographies in 1998 and in 1999, the elevation of the river bed was 2 m lower because flow capacity in this section was enlarged after the disasters [Kobe Shimbun (news paper), 1999d]. In the 1998 flood, the river section was under repair and temporary structures were built in the river section. These structures were gradually destroyed during the flood, and debris and driftwood became lodged around the structures, so the actual state of river section is unknown. Due to the uncertainties in the profile and flow capacity reduction of the river section in 1998, flow in the river cross-section is not calculated, but the overflow hydrograph at the south side of the Senshin Bridge (Fig. 13) is used as the inflow boundary condition in the 1998 disaster calculation. To estimate the disaster in 1999, topography including the river section is represented in the calculation grid and both river flow and inundation flow are calculated in the flow model. At the upstream boundaries of the Ishii River and the Ten-nodani River in the domain, the observed hydrograph [Yoshida, 2000] shown in

Fig. 15 is used as the boundary condition. Water level used as the outflow boundary condition was calculated by one dimensional varied flow calculation by the comitte of the Shin-minato river flood [1998].

Fig. 16 shows the calculation grid used in this section. One hundred thousand nodal points and 134,000 triangles are used in the grid. The average grid size is about 5 m. To discuss the sensitivity of grid size to the estimated flow structure, coarser grids with grid sizes of 8 m, 10 m and 12 m are also generated.

3.2.2. Results and discussion In Fig. 17, the sensitivity of grid size to the time-series expansion of the inundation area and local water depths of 1998 inundation condition are shown. The locations of two measuring points are depicted in Fig. 16c. For the time-series variation of the inundated area, the result shows approximately the same profile, so the sensitivity of the grid size to the inundated area seems to be definitive. This means that to predict the maximum extent of inundation, a very fine grid is not necessary but the order of 10 m is sufficient. However, in Fig. 17a, the results of coarser grids (10 m and 12 m) seem to be overestimated slightly compared with results of finer grids (5 m and 8 m). This is because topographical features of both elevation distribution and building arrangement are simplified or have poor representation in a coarser grid, and those errors yield over diffusion of inundation flow in complicated topography [Tsubaki et al., 2007]. This tendency exerts the local water depth. As shown in Fig. 17b and Fig. 17c, coarser grid results (8 m to 12 m) underestimate the water depths at the measuring points located in streets. In urban areas, streets have comparatively low elevation due to the drainage efficiency and smooth traffic of vehicles. This means that the resolution of topographical features becomes finer; especially in the case of shallow water depth, the inundation flow concentrates on the street more, and the water depth of the street is estimated to be deeper. In the following analysis, a grid size of 5 m is used to resolve

local flow characteristics precisely.

The estimated inundation that occurred in 1998 is shown in Fig. 18. In this figure, water depth distributions at 4 different times are shown and an overflow (inflow) hydrograph is shown in Fig. 18e. the inundated area spreads concentrically at the initial phase (Fig. 18a–b), and subsequently because of the local high elevation of the former river path, the propagation front of the inundation flow is divided into two parts; one that goes to the south, and another that goes to the south-east (Fig. 18c–d). A certain amount of inundated water volume remains around the overflow point; however, due to the slope of ground surface, the front of the inundation spreads along the complex road network and causes local inundation at an area far from the overflow point (Fig. 18d). The inundated area shown in Fig. 18d corresponds in general to the inundated area in an actual disaster record shown in Fig. 13. In the numerical estimation of the 1998 inundation, the inflow boundary condition is configured at the left bank of the river (south side of the river in Fig. 18). Consequently, the small inundation of the north part of river is not represented in the estimation and the water volume, which inundated in the north part, is dispatched to the south part, so the south part inundation is overestimated in a measure. The recorded water depth of the inundation is about 1 m or more [Kobe Shimbun (news paper), 1998], and the calculated inundated water depth around overflow point is about 1.5 meters. Although quantitative information on the actual disaster is limited, the calculated results agree well with the situation of the actual disaster except for small differences in the inundated area caused by the boundary condition uncertainty. Therefore, it may be said that the developed approach including grid generation is reliable for estimation of urban inundation disasters. To estimate 1.4 hours of inundation flow, it takes 8.5 hours of calculation using a PC with the AMD Phenom 9550 CPU with a frequency of 2.6 GHz.

Second, the calculated results of the inundation disaster in 1999 are shown in Fig. 19. In this case, hydrographs at the Shin-minato river tributaries are used as the inflow boundary condition. The total discharge of the inflow hydrographs is shown in Fig. 15. The peak flow rate of 160 m^3/s occurred at t = 18:00 and overflow from the river started from t = 17:40. Overflow from the areas around the Senshin Bridge (point X in Fig. 19a) and around the upper mouth of the Egeyama Tunnel (point Y in Fig. 19a) is observed in Fig. 19. During a time period from t = 17:40 to t = 18:00, the inundation area spreads besides the river around the overflow points. After t = 18:00 (peak discharge of river flow), the inundation spreads southward. The inundated area expands rapidly along with the road network, and the inundated water depth in the expanded area is comparatively shallow. The road network is comparatively flat and has small slope change; therefore, the inundated water spread rapidly, and its water depth became shallow. Inundated areas are generally the same as in the actual case of the 1998 flood and agree well with the actual inundated area shown in Fig. 13, supporting the good performance of the present method of inundation simulation.

3.3. Summary of the Shin-minato River inundation estimation

In this section, inundation disasters that occurred in the catchment area of the Shin-Minato River are discussed, considering detailed topographical information using the method developed herein. The topographical situation of the river and disasters that occurred in this catchment are described, and then the inundation disasters that occurred in 1998 and 1999 are simulated. The inundation flow propagates with a complex pattern, which agrees with the actual situation in general. Inundation flow structure is explored, discussing the global features and details of the geospatial situations of this area. The inundation propagation in the Shin-minato River basin is strongly influenced by the catchment topography, especially the former river path.

The elevation around the present river and the former river path are locally high compared with the surrounding area. Consequently, overflow water rapidly spreads toward comparatively lower areas and becomes trapped in the depressed topography. Expansion of inundation is separated by the old river path and spreads following the road network.

4. Conclusion

In this study, a method for detailed inundation estimation for an urbanized area resolving land features obtained by LiDAR is developed. This approach distinguishes buildings from vegetation and treats them differently in the model, as wall boundaries for buildings and a roughness for vegetation, respectively. The unstructured grid is generated to represent the building shapes precisely. The accuracies of grids with different grid sizes and grid types are compared and the optimal range of the grid spacing for direct representation of the urban topography is proposed. Using this method, inundation disasters that occurred in the Shin-minato River basin are estimated. Detailed flow structures are represented in the numerical model, and flow characteristics are discussed with respect to the land features of the site.

Acknowledgments

This study was made possible by a grant from the Research Center for Urban Safety and Security, Kobe University. The authors would also like to thank Asian Air Survey Co., ltd. for supporting LiDAR measurements. The authors are deeply grateful to Emeritus Prof. Takeshi Kawatani of Kobe University for helping with this study.

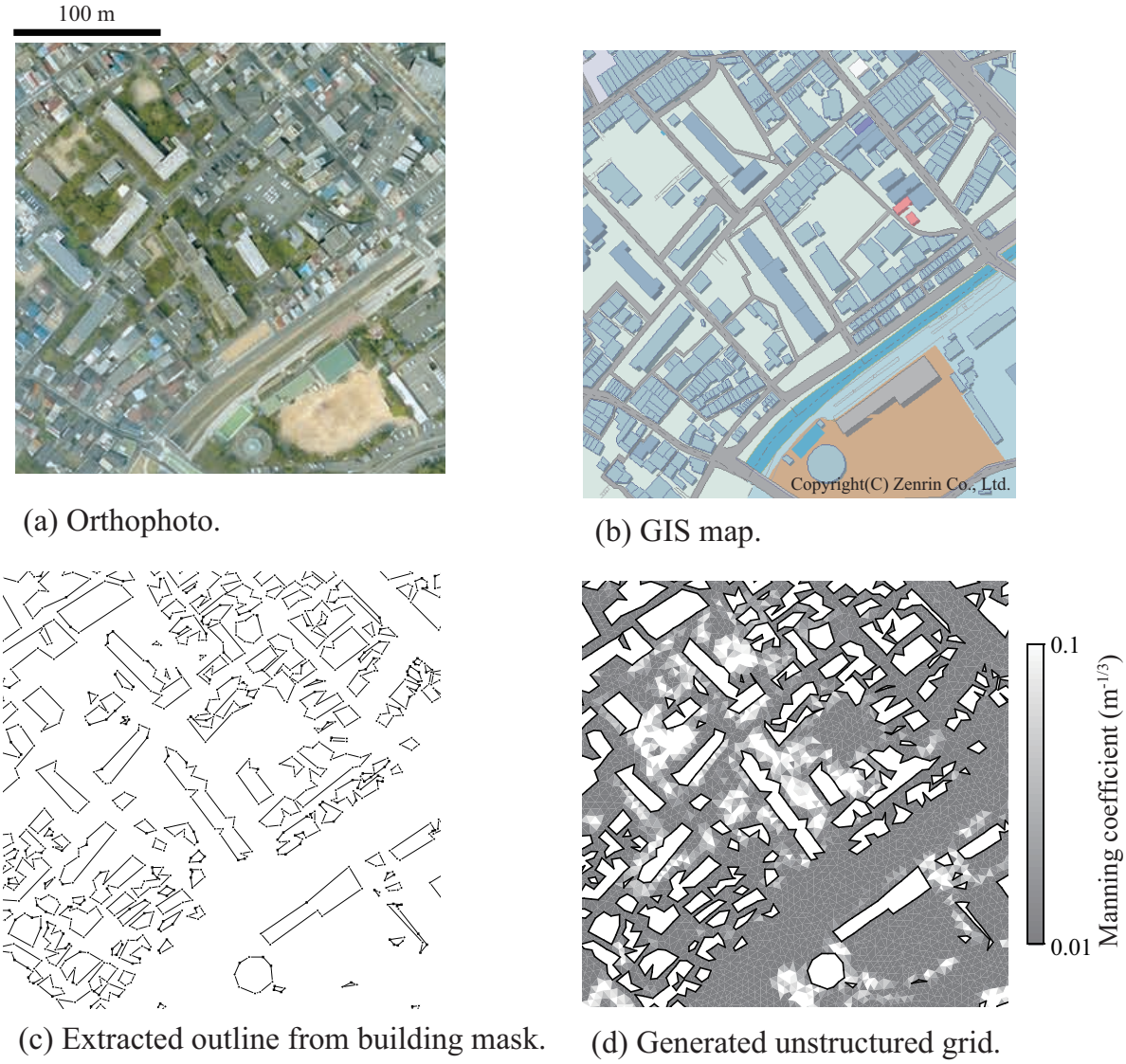

(a) Orthophoto.

(b) GIS map.

(c) Extracted outline from building mask.

(d) Generated unstructured grid.

Figure 7. Sample of building extraction and unstructured grid generation. GIS map is based on Zenrin electronic map Z8 distributed by Zenrin Co., Ltd., Japan.

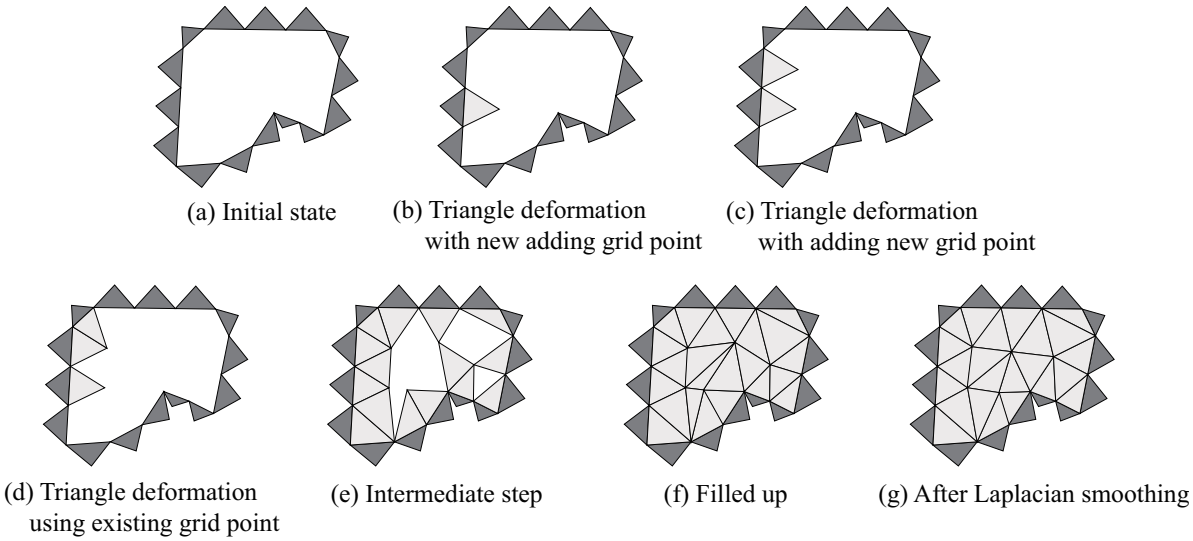

Figure 8. Schematic of advancing front method.

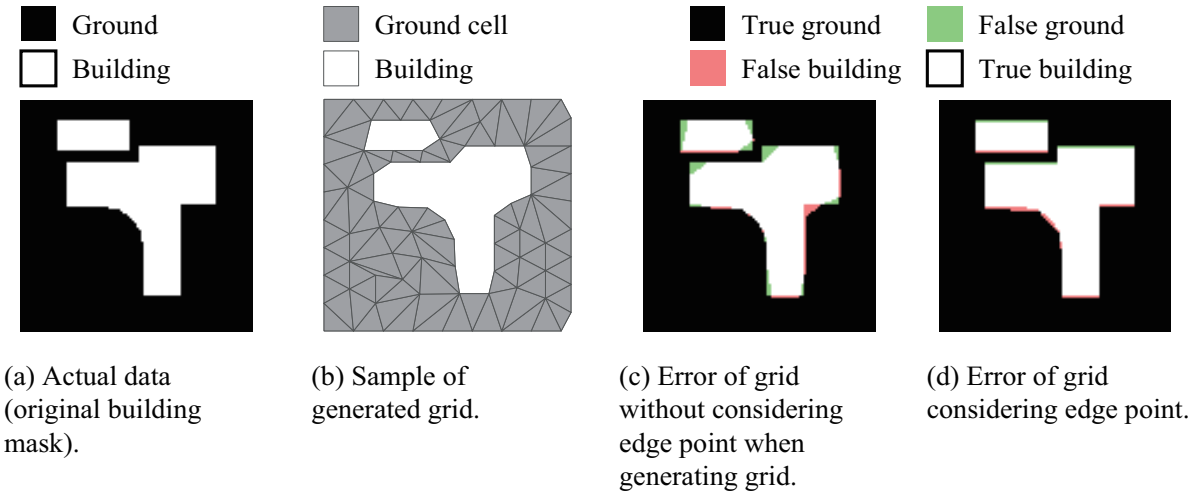

Figure 9. Sample of correct building raster, generated grid sample, and error of two different sample grids.

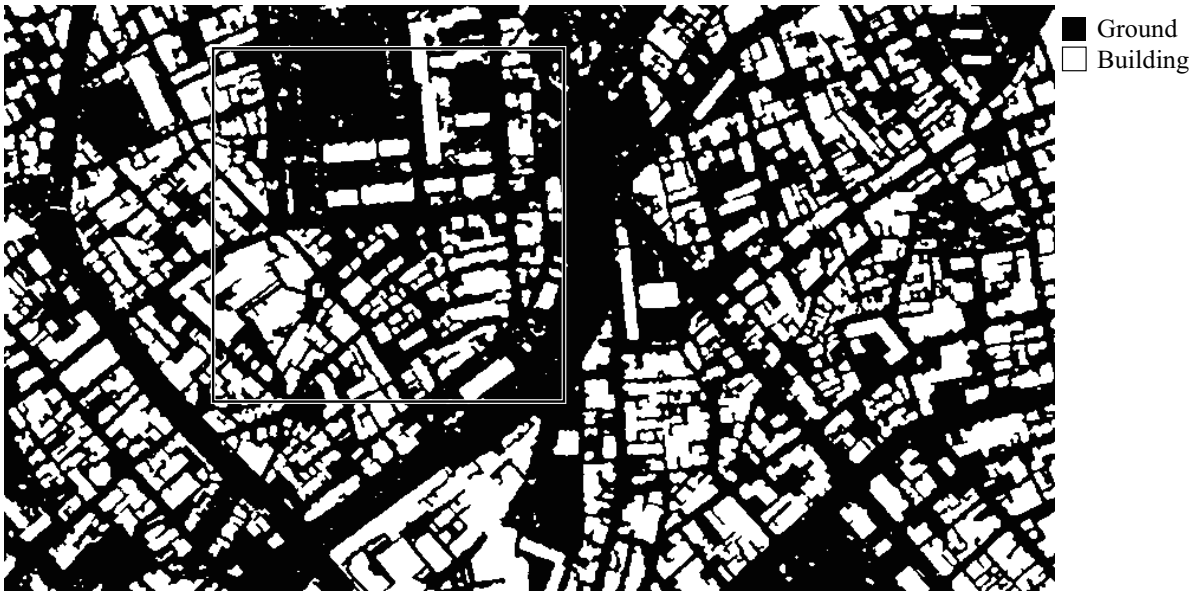

Figure 10. Domain used to evaluate grid accuracy. Domain size is 889 by 495 meters. The building area occupies 36.6 percent of the entire domain. In Fig. 11, a close-up of the square region in this figure is shown.

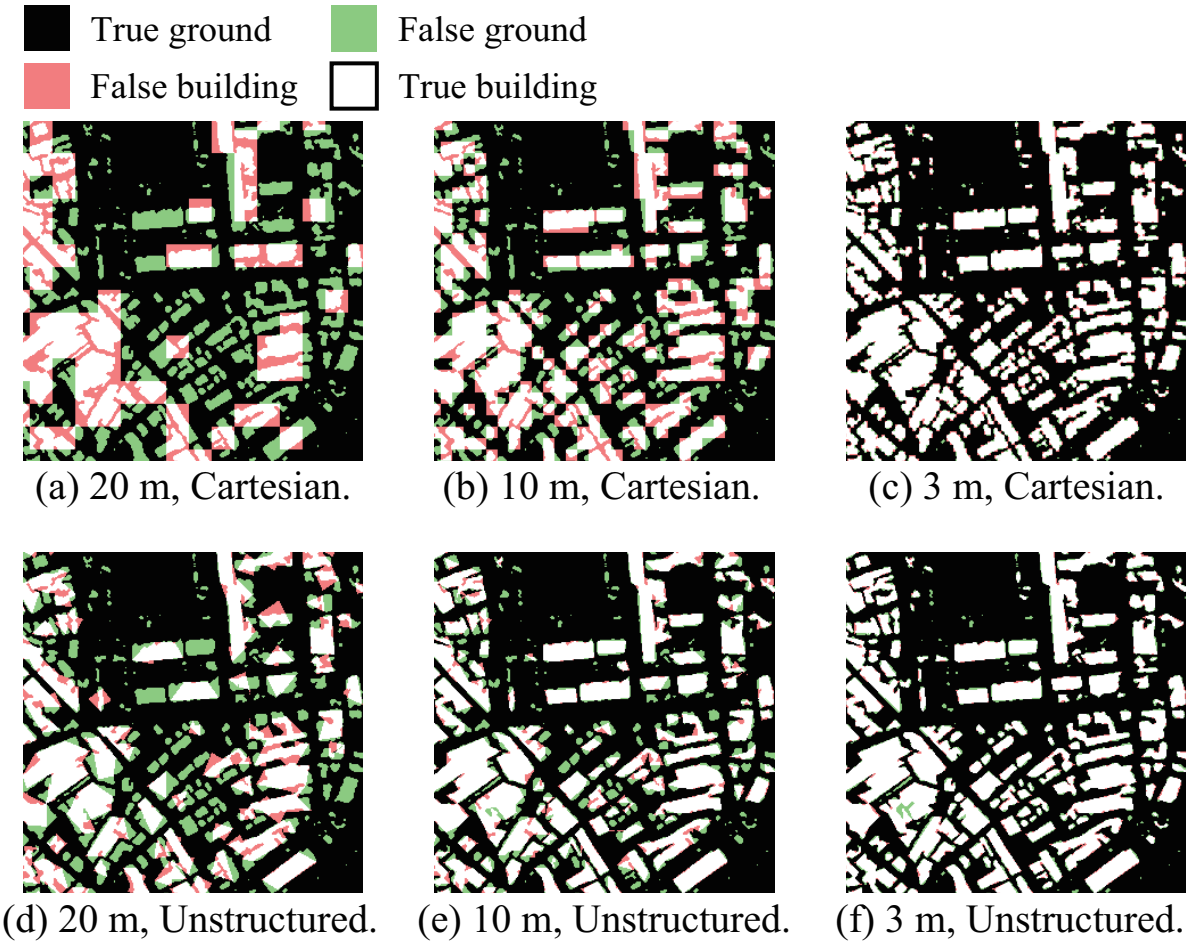

Figure 11. Horizontal errors for different grid sizes and grids type. A 300 by 300 meter region within Fig. 10 is selected for each case to compare differences.

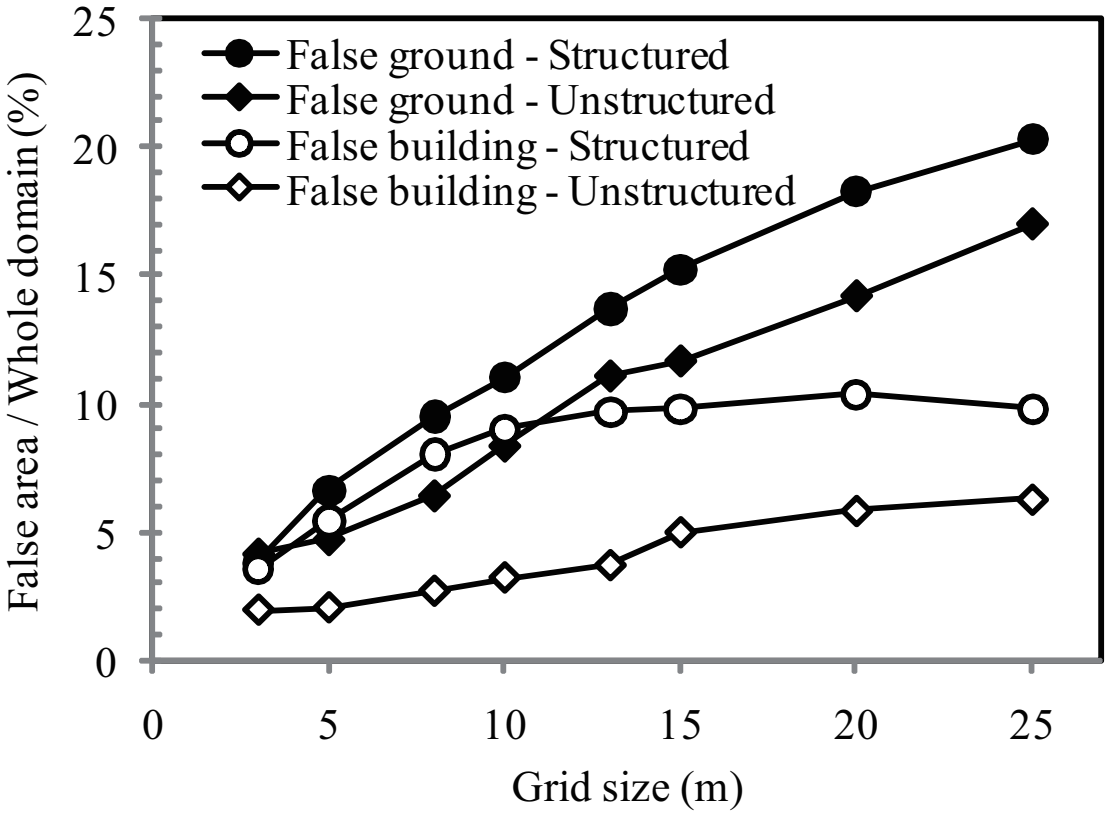

Figure 12. Grid error.

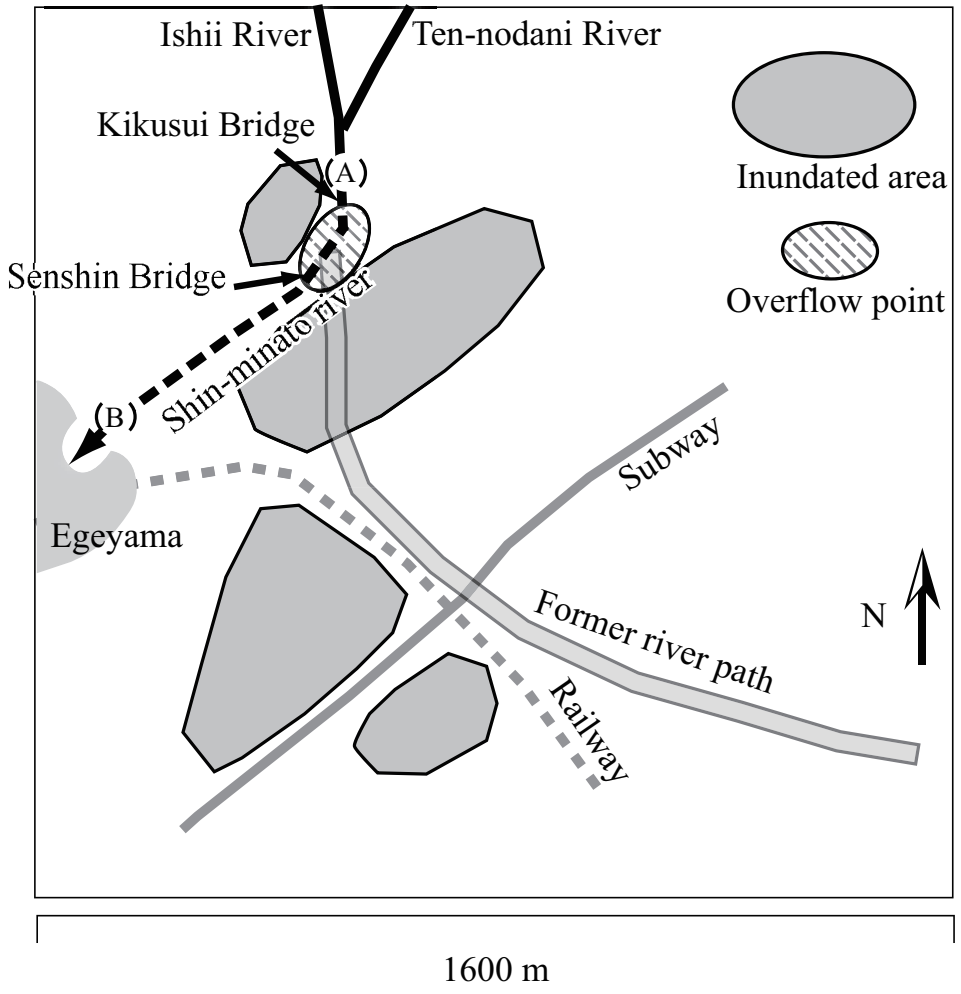

Figure 13. Inundated area in 1998 and 1999 due to overflow from Shin-minato RiverKobe Shimbun (news paper) [1999b].

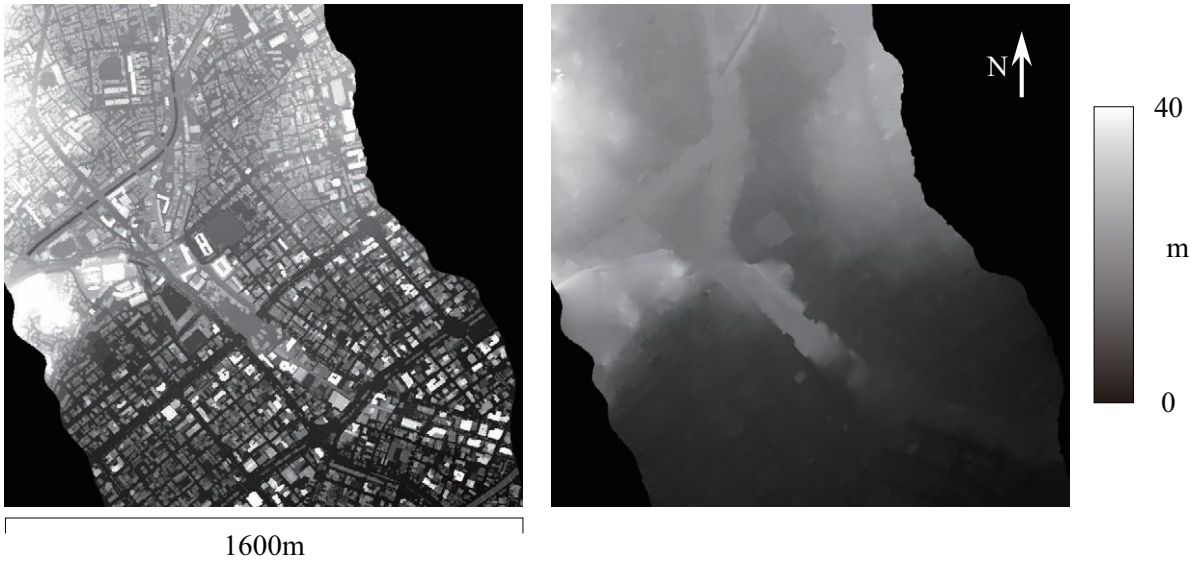

(a) Digital surface model. (b) Digital elevation model.

Figure 14. Topography around inundated area of Shin-minato river basin. Summary of geographical features in this area is shown in Fig. 13.

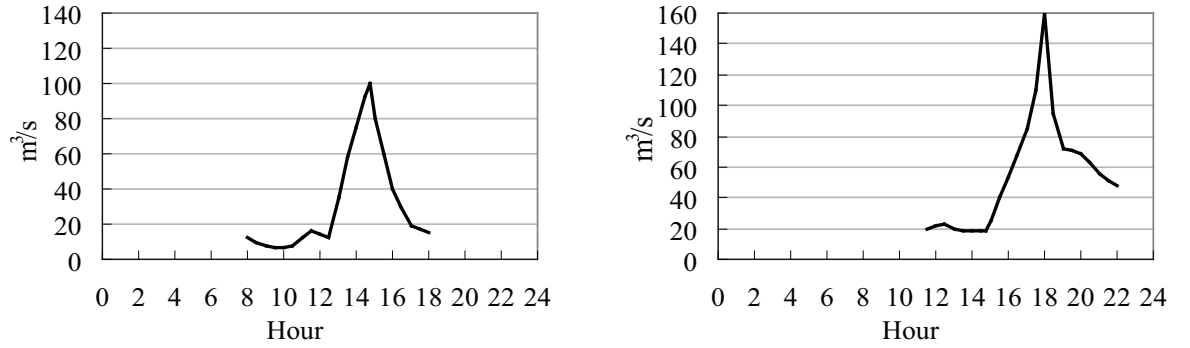

(a) Hydrograph during flood on August 22nd, 1998.

(b) Hydrograph during flood on June 29th, 1999.

Figure 15. Measured flow rate of Shin-minato river near overflow point.

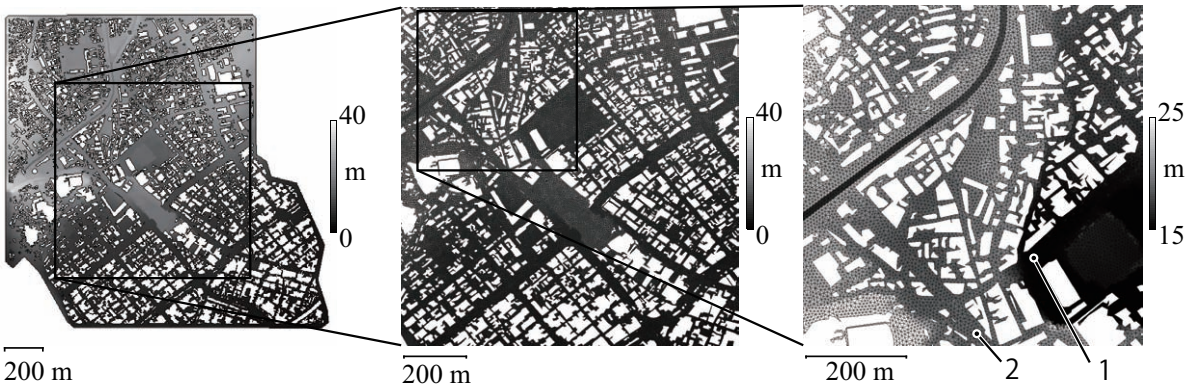

(a) Whole domain.

(b) Closeup of inundated area.

(c) More detailed closeup.

Figure 16. Calculation grid with elevation contour. Point 1 and point 2 in (c) show locations of measurement points.

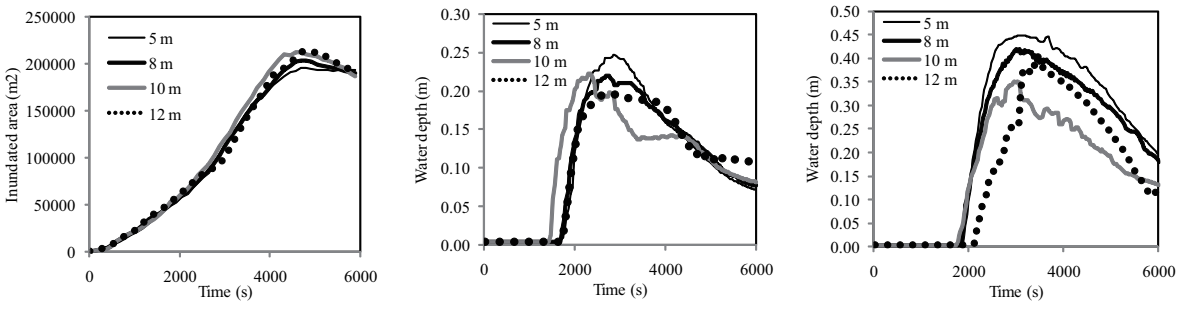

(a) Inundated area

(b) Water depth at point 1

(c) Water depth at point 2

Figure 17. Sensitivity of grid size on time-series quantities.

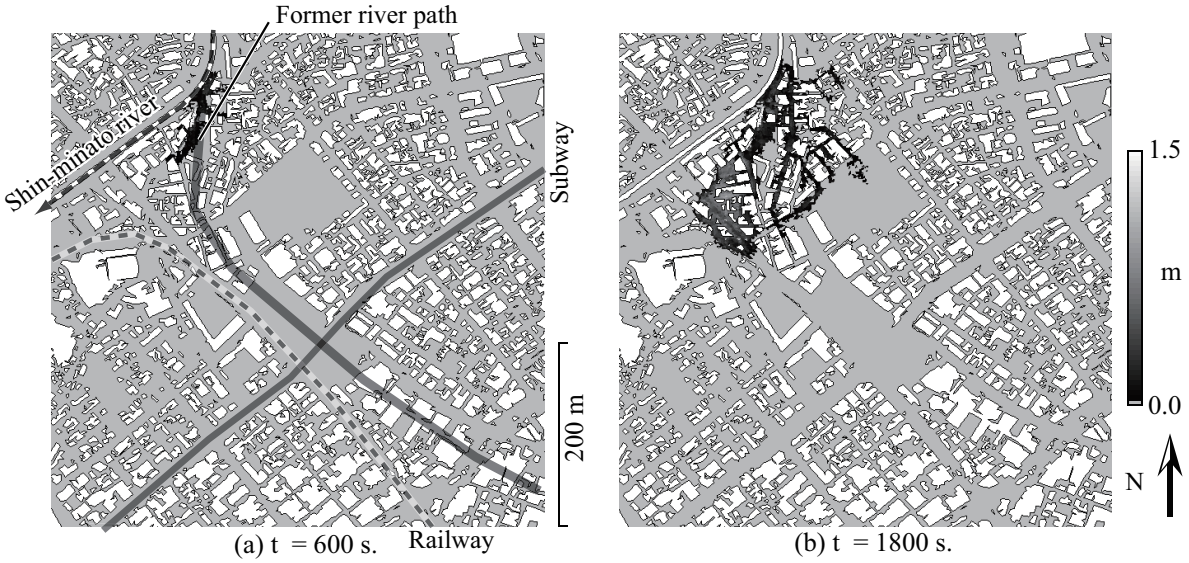

(a) t = 600 s.

(b) t = 1800 s.

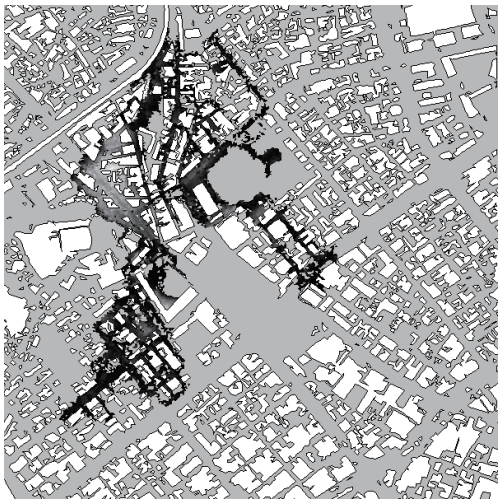

(c) t = 3200 s.

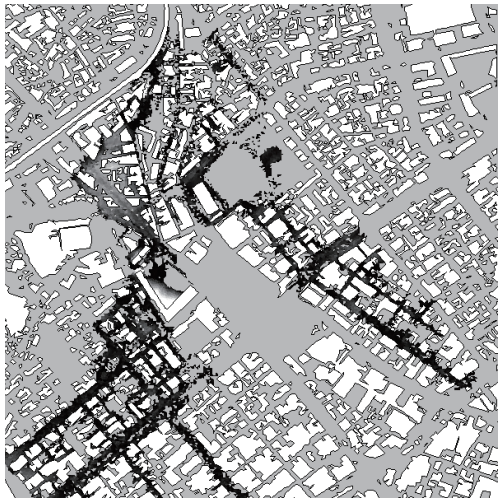

(d) t = 4600 s.

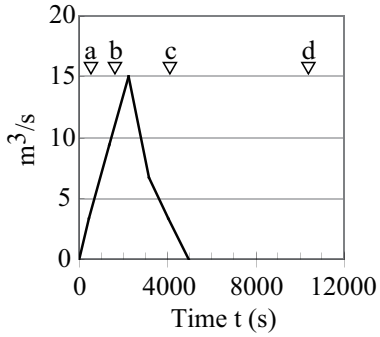

(e) Hydrograph of overflow from river.

Figure 18. Estimated water depth in 1998 case. Markers a-d depicted in figure e indicate the timings of snap shots shown in figures a-d.

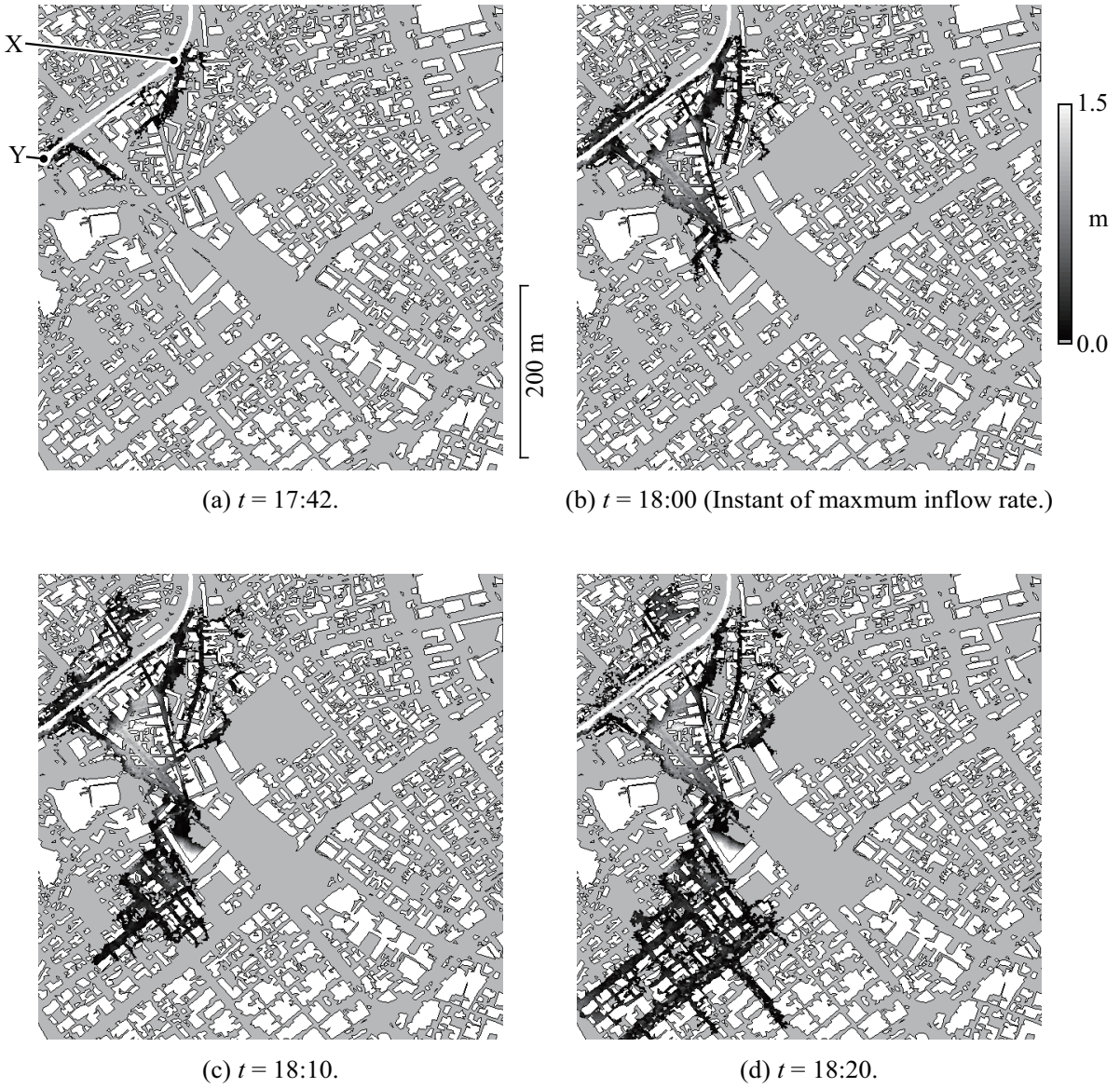

(a) t = 17:42.

(b) t = 18:00 (Instant of maxmum inflow rate.)

(c) t = 18:10.

(d) t = 18:20.

Figure 19. Estimated water depth in 1999 case. X and Y indicate locations of the Senshin Bridge and the upper region of Egeyama Tunnel respectively.

References

F. Alcrude and P. Garcia-Navarro. A high-resolution godunov-type scheme in finite volumes for the 2D shallow-water equations. 16:489–505, 1993.

K. Anastasiou and C. T. Chan. Solution of the 2D shallow water equations using the finite volume method on unstructured triangular meshes. *International Journal for Numerical Mehtods in Fluids*, 24:1225–1245, 1997.

M.-F. Auclair-Fortier, D. Ziou, C. Armenakis, and S. Wang. Survey of work on road extraction in aerial and satellite images. Tech. rep., Departement de mathematiques et d'informatique, Universite de Sherbrooke, 2000.

P. D. Bates. Remote sensing and flood inundation modelling. *Hydrological processes*, 18:2593–2597, 2004.

P. D. Bates, K. J. Marks, and M. S. Horritt. Optimal use of high-resolution topographic data in flood inundation models. *Hydrological processes*, 17:537–557, 2003.

J. Brasington and K. Richards. Reduced-complexity, physically-based geomorphological modelling for catchment and river management. *Geomorphology*, 90:171–177, 2007.

C. Brenner. Building reconstructuion from images and laser scanning. *International Journal of Applied Earth Observation and Geoinformation*, 6:187–198, 2005.

S. A. Canann, J. R. Tristano, and M. L. Staten. An approach to combined Laplacian and optimization-based smoothing for triangular, quadrilateral, and quad-dominant meshes. In *Proceedings of the 7th international meshing roundtable*, pages 479–494, 1998.

S. Clode and F. Rottensteiner. Classification of trees and powerlines from medium resolution airborne laserscanner data in urban environments. In *APRS Workshop on Digital Image Computing*, Brisbane, 2005.

D. M. Cobby, D. C. Mason, M. S. Horritt, and P. D. Bates. Two-dimensional hydraulic flood modelling using a finite-element mesh decomposed according to vegetation and topographic features derived from airborne scanning laser altimetry. *Hydrological processes*, 17:1979–2000, 2003.

I. comitte of the Shin-minato river flood. Hazard report of the shin-minato river flood. Technical report, 1998.

D. Djokic and D. R. Maidment. Terrein analysis for urban stormwater modelling. *Hydrological processes*, 5(1):115–124, 1991.

D. A. Field. Laplacian smoothing and Delaunay triangulations. *Commnications in Applied Numerical Methods*, 4:709–712, 1988.

H. A. Gallegos, J. E. Schubert, and B. F. Sanders. Two-dimensional, high-resolution modeling of urban dam-break flooding: A case study of baldwin hills, california. *Advances in Water Resources*, 32(8):1323–1335, Aug. 2009.

H. Kaartinen et al. (twelve authers). Accuracy of 3D city models: EuroSDR comparison. In *ISPRS working group III/3, III/4, V/3 Workshop "Laser scanning 2005"*, pages 227–232, Netherlands, Sept. 2005.

K. A. Hoffmann and S. T. Chiang. *COMPUTATIONAL FLUID DYNAMICS FOR ENGINEERS*, volume II. Engineering Education System, 1993.

N. M. Hunter, P. D. Bates, S. Neelz, G. Pender, I. Villanueva, N. G. Wright, D. Liang, R. A. Falconer, B. Lin, S. Waller, A. J. Crossley, and D. C. Masoc. Benchmarking 2d hydraulic models for urban flooding. *Water Management*, 161:13–30, 2008.

Hyogo prefecture, Japan. *Agenda of river control planof the Shin-minato river system.* Hyogo prefecture, Japan, 2000.

Hyogo prefecture, Japan. *Master plan of river control of the Shin-minato river system.* Hyogo prefecture, Japan, 2001.

S. N. Jonkman and J. K. Vrijling. Loss of life due to floods. *Journal of Flood Risk Management*, 1:43–56, 2008.

M. Kaneko, M. Igor, and Y. Nakamura. *Instruction for Automatic Generation of Three Dimensional Unstructured Grid Program.* Computational research center, Nagoya University, 2000.

Kobe Shimbun (news paper). *Sept. 23th, morning edition.* Kobe Shimbun Co., Ltd., 1998.

Kobe Shimbun (news paper). *Aug. 1st, morning edition.* Kobe Shimbun Co., Ltd., 1999a.

Kobe Shimbun (news paper). *Jul. 1st, morning edition.* Kobe Shimbun Co., Ltd., 1999b.

Kobe Shimbun (news paper). *Jul. 2nd, evening edition.* Kobe Shimbun Co., Ltd., 1999c.

Kobe Shimbun (news paper). *Jun. 30th, evening edition.* Kobe Shimbun Co., Ltd., 1999d.

S. H. Lo. A new mesh generation scheme for arbitrary planar domains. *International Journal for Numerical Methods in Engineering*, 21(8):1403–1426, 1984.

S. H. Lo. Finite element mesh generation and adaptive meshing. *Prog. Struct. Engng Mater.*, 4:381–399, 2002.

O. Mark, S. Weesakul, C. Apirumanekul, S. B. Aroonnet, and S. Djordhević. Potential and limitaions of 1d modelling of urban flooding. *Journal of Hydrology*, 299(3–4): 284–299, 2004.

D. C. Mason, D. M. Cobby, M. S. Horritt, and P. D. Bates. Floodplain friction parameterization in two-dimensional river flood models using vegetation heights derived from airborne scanning laser altimetry. *Hydrological processes*, 17:1711–1732, 2003.

D. C. Mason, M. S. Horritt, N. M. Hunter, and P. D. Bates. Use of fused airborne scanning laser altimetry and digital map data for urban flood modelling. *Hydrological processes*, 21:1436–1447, 2007.

H. K. McMillan and J. Brasington. Reduced complexity strategies for modelling urban floodplain inundation. *Geomorphology*, 90:226–243, 2007.

C. on Hydroscience and J. Hydraulic Engineering. *Hydraulic formulae*. JSCE, 2000.

S. J. Owen. A survey of unstructured mesh generation technology. In *Proceedings of 7th International Meshing Roundtable*, pages 239–267, Mearborn, 1998.

G. Priestnall, J. Jaafar, and A. Duncan. Extracting urban features from LiDAR digital surface models. *Computers, Environment and Urban Systems*, 24:65–78, 2000.

S. Rath and B. Bajat. Between sensing, forecasting and risk assessment: An integrated method to model high resolution data for floodplain representations in hydrodynamic simulations. In *Proc. 1st Goettingen Remote Sensing Days*, Goettingen, Oct. 2004.

F. Rottensteiner, H. Kager, C. Briese, and K. Kraus. LIDAR activities at the viennese institute of photogrammetry and remote sensing. In *3rd Int. LIDAR workshop*, Columbus, 2002.

F. Rottensteiner, J. Trinder, S. Clode, and K. Kubik. Building detection using LiDAR data and multi-spectral images. In *VIIth Digital image computing*, pages 673–682, Sydney, 2003.

A. Sampath and J. Shan. Building boundary tracing and regularization from airborne lidar point clouds. *Photogrammetric Engineering & Remote Sensing*, 73(7):805–812, Jul. 2007.

B. F. Sanders, J. E. Schubert, and H. A. Gallegos. Integral formulation of shallow-water equations with anisotropic porosity for urban flood modeling. *Journal of Hydrology*, 362:19–38, 2008.

J. E. Schubert, B. F. Sanders, M. J. Smith, and N. G. Wright. Unstructured mesh generation and landcover-based resistance for hydrodynamic modeling of urban flooding. *Advances in Water Resources*, 31:1603–1621, 2008.

M. Shige-eda and J. Akiyama. Numerical and experimental study on 2D flood flows with and without structures. *Journal of Hydraulic Engineering*, 129(10):817–821, 2003.

M. Shigeda, J. Akiyama, M. Ura, A. K. Jha, and Y. Arita. Numerical simulations of flood propagation in a flood plain with structures. *Journal of Hydroscience and Hydraulic Engineering*, 20(2):117–129, 2002.

G. Sithole and G. Vosselman. Automatic structure detection in a point cloud of an urban landscape. In *2nd GRSS/ISPRS Joint Workshop on Remote Sensing and Data Fusion over Urban Areas*, pages 67–71, Berlin, 2003.

P. Tamamidis and D. N. Assanis. Evaluation of various high-order-accuracy schemes with and without limiters. *International Journal for Numerical Mehtods in Fluids*, 16:931–948, 1993.

S.-H. Teng and C. W. Wong. Unstructured mesh generation: Theory, practice, and perspectives. *International Journal of Computational Geometry and Applications*, 10:227–266, 2000.

G. Testa, D. Zuccala, F. Alcrude, J. Mulet, and S. Soares-Frazao. Flash flood flow experiment in a simplified urban district. *Journal of Hydraulic Research*, 45:37–44, 2007.

R. Tsubaki, I. Fujita, and T. Okabe. Sensitivity of grid spacing to prediction and coherent flow structure of inundation on urban area. In *32nd confress of IAHR*, Venice, Italy, July 2007.

G. Vosselman. 3D reconstruction of roads and trees for city modelling. In *ISPRS working group III/3 workshop*, Dresden, 2003.

J. Wang and R. Liu. The composite finite volume method on unstructured meshes for the two-dimensional shallow water equations. *International Journal for Numerical Mehtods in Fluids*, 37:933–949, 2001.

Q. Weng and D. A. Quattrochi, editors. *Urban remote sensing*. CRC Press, 2006.

D. A. Woolhiser, R. E. Smith, and D. C. Goodrich. KINEROS, a kinematic runoff and erosion model. Documentation and user manual, US Department of Agricultural Research Service, Tucson, Arizona, 1990.

T. Yoshida. Runoff analysis using tank model. OGI technical reports, Ohyo gijyutu Co., Ltd., 2000.

D. Yu and S. N. Lane. Urban fluvial flood modeling using a two-dimensional diffusion-wave treatment, part 1: mesh resolution effects. *Hydrological processes*, 20(7):1541–1565, 2006a.

D. Yu and S. N. Lane. Urban fluvial flood modelling using a two-dimensional diffusion-wave treatment, part 2: development of a sub-grid-scale treatment. *Hydrological processes*, 20(7):1567–1583, 2006b.